PNAS
www.pnas.org

Supplementary Information for

Phase transforming metamaterial with magnetic interactions

Xudong Liang[1, 2, *], Hongbo Fu[1], Alfred J. Crosby[1, *]

[1] Polymer Science and Engineering Department, University of Massachusetts Amherst, Amherst, MA, 01003, USA
[2] School of Science, Harbin Institute of Technology (Shenzhen), Shenzhen 518055, China

*Xudong Liang
Email: liangxudong@hit.edu.cn

*Alfred J. Crosby
Email: acrosby@umass.edu

This PDF file includes:
Supplementary text
Figures S1 to S21
Tables S1 to S2
SI References

Other supplementary materials for this manuscript include the following:
Movies S1 to S5

Supplementary Information Text

1. Fabrications

The metamaterials investigated in this study are fabricated on a polyurethane sheet (PU 40A; McMaster-Carr) with thickness h=3.18 mm, Young's modulus E_0=1.68 MPa (shear modulus μ_0=0.56 MPa), and Poisson's ratio v_0=0.49. The internal structures are laser cut with a 30 W CO_2 laser (Universal Laser System, VSL 3.5). Vector cutting is performed at 100% power and 25% speed. As shown in Fig. S1, the shapes of periodically distributed and orthogonally aligned pores are controlled by the geometrical parameters (a_0, b_0, and w_0 in Fig. S1b) in Table S1. The remained periodic structures resemble a series of plates connected by slender, flexible ligaments (Fig. S1a). The length of a representative unit, $L_0=w_0+b_0+a_0$, is fixed as 6 mm. The diameter of pores to hold the magnets is d_0 ~2.9 mm, smaller than the one of magnets (d=3.1 mm). The laser cutting resolution is about ±0.25 mm, and the geometrical parameters are included in Table S1.

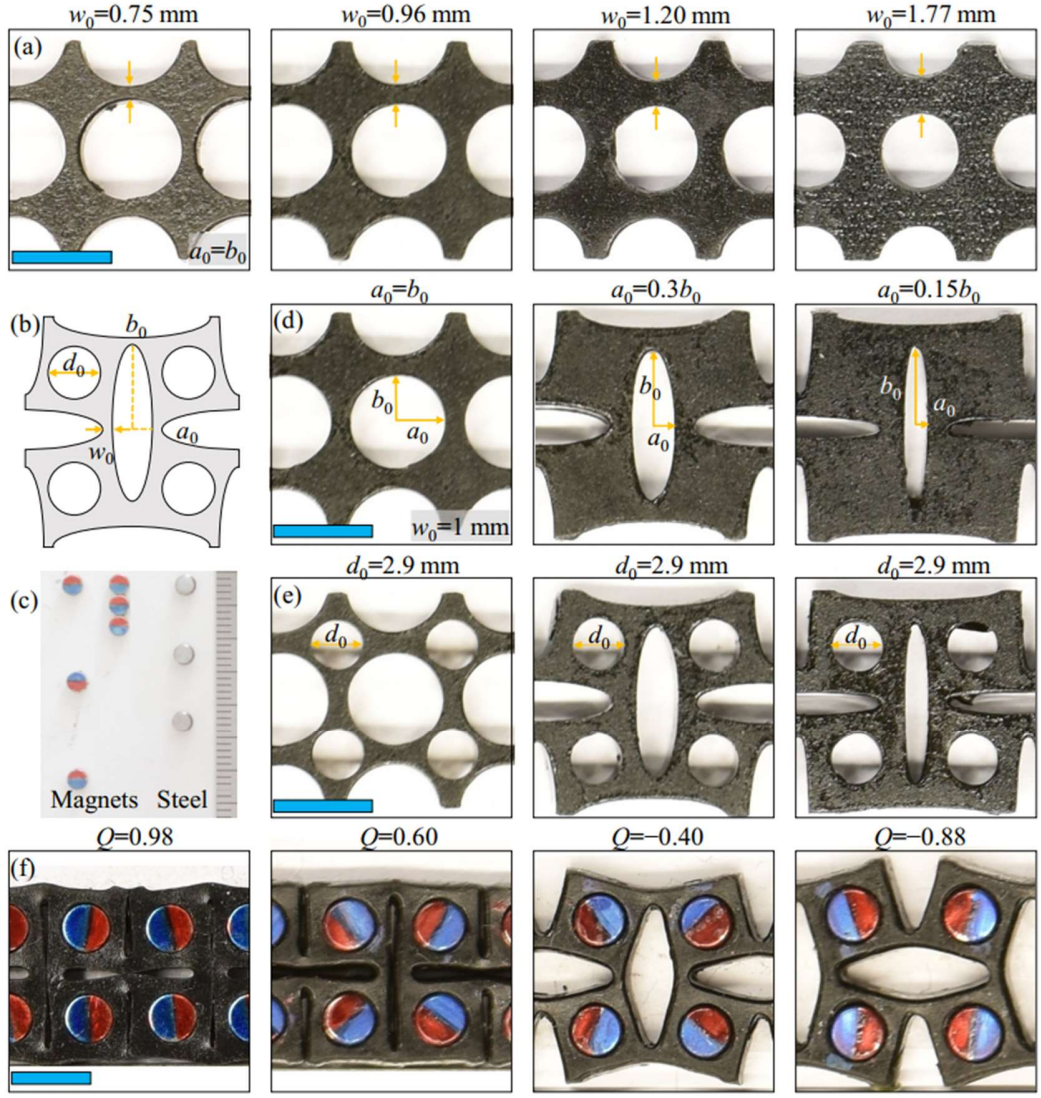

Figure S1. (a) Mechanical metamaterials with different ligament widths w_0. (b) Schematic of the geometry of metamaterials with pores. (c) Non-interacting steel cylinders and interacting cylindrical magnets that are magnetized through the diameter. The south and north pole are colored red and blue, respectively. (d) Mechanical metamaterials with different pore aspect ratios a_0/b_0. (e) Metamaterials with extra pores at the center of the plates to hold the magnets. (f) Elasto-magnetic metamaterials with different magnet orientations. Scale bar, 5 mm.

Table S1 Geometrical parameters for the metamaterial structure

w_0 (mm)	a_0, b_0 (mm, mm)
0.79±0.07	(2.57±0.02, 2.63±0.04); (1.37±0.05, 3.83±0.04); (0.75±0.04, 4.44±0.06);
0.99±0.08	(2.46±0.02, 2.50±0.02); (1.05±0.04, 3.90±0.05); (0.62±0.04, 4.26±0.05);
1.23±0.06	(2.34±0.03, 2.38±0.03); (1.63±0.04, 3.12±0.02); (0.62±0.03, 4.03±0.05);
1.71±0.06	(2.09±0.03, 2.11±0.03); (1.08±0.03, 3.06±0.04); (0.61±0.04, 3.53±0.03).

Two types of metamaterials are fabricated in this study: metamaterials without magnetic domains (Fig. S1a and S1d) and metamaterials with magnetic or stainless steel domains (Fig. S1e and S1f). We refer to the former as mechanical metamaterials and the latter as elasto-magnetic metamaterials. The static and dynamic responses of elasto-magnetic metamaterials are compared with the mechanical metamaterials in this study. The mechanical responses in the mechanical metamaterials are geometrically controlled by the ligament width w_0 and the pore aspect ratio a_0/b_0, according to our previous works (1,2).

The interacting magnets are embedded in the metamaterial (Fig. S1e). The magnets are magnetized through the diameter, with the south and north pole colored red and blue, respectively (Fig. S1c). The magnetic interactions are controlled via the magnetic moment (oriented from the south to the north pole), and its angle with the y-axis is θ_i (Fig. 1a). We define an orientational parameter $Q=\cos(\theta_i)\cos(\theta_{i+1})$ in the configuration free from external loads, ranging from –1 to 1 to represent the magnetic interactions' relative strength. The neighboring magnets are repulsive as $Q<0$ and switch to be attractive as $Q>0$. Steel pins with the same shape and density as the magnets are used in elasto-magnetic metamaterials, representing the non-interacting conditions with $Q=0$. The magnets' orientations with respect to the y-axis are constrained by the frictional forces in the surrounding polymer in fabrication. We embed the magnets with different orientations to create elasto-magnetic metamaterials with various magnetic interactions, ranging from attractive to repulsive (Fig. S1f).

The insertion of magnets and steel pins in the metamaterials also changes the samples' initial length before applying external loads (Fig. 1c and 1d). We take the mechanical metamaterials as a reference (Fig. S1a and S1d), of which the representative length is L_0=6 mm, and the length between the centers of the first and last plates is l_0=114 mm. We measure the sample length l after inserting the magnets or steel pins in elasto-magnetic metamaterials. The attractive (repulsive) magnets shorten (elongate) the metamaterials. The steel cylinders slightly increase the metamaterials' length due to the frustrations in assembly. Table S2 shows the changes in the initial length for elasto-magnetic metamaterials with different internal structure geometry (w_0/L_0 and a_0/b_0) and magnetic moment orientations (Q). Elasto-magnetic metamaterials with elliptical pores ($a_0/b_0<<1$) shorten (elongate) substantially with the attractive (repulsive) magnets, while the ones with circular pores (a_0/b_0~1) barely change their lengths.

Table S2 Change of initial lengths in elasto-magnetic metamaterials, $(l-l_0)/l_0$

w_0/L_0 and a_0/b_0	Q~1	Q~0.5	Q~0	Q~−0.5	Q~−1
(0.13, 0.95)	0.038	−	0.046	−	−
(0.13, 0.36)	-0.192	−	0.046	−	0.115
(0.14, 0.17)	-0.115	-0.077	0.038	0.138	0.154
(0.16, 0.97)	0.031	−	0.046	−	0.054
(0.16, 0.27)	-0.138	-0.085	0.046	0.092	0.092
(0.17, 0.17)	-0.077	-0.075	0.031	0.100	0.108
(0.20, 0.96)	0.023	−	0.046	−	0.054
(0.20, 0.52)	-0.008	−	0.038	−	0.062
(0.21, 0.15)	-0.069	0.031	0.031	0.077	0.092
(0.28, 0.97)	0.023	−	0.038	−	0.046
(0.29, 0.35)	0.008	−	0.031	−	0.054
(0.29, 0.17)	-0.015	−	0.038	−	0.054

2. Experiments

2.1 Quasi-static uniaxial tensile

The quasi-static constitutive responses of metamaterials are studied using a tensile tester (Instron 5564). The metamaterials are loaded by pins through the holes fabricated at the top and bottom edges (Fig. S2a, left), ensuring a pin boundary condition. The pins are attached to an acrylic plate held by pneumatic grips (working pressure, 70 psi). We also measure the forces between the interacting magnets through screw grips (Fig. S2a, right) on a texture analyzer (Stable Micro Systems, TA.XT plusC). The forces in all tests are measured with a 50 N load cell with 1 mN resolution. All tests are conducted at a speed of 1 mm/s.

We show the force-displacement relations between the attractive magnets (Q=1) and the mechanical metamaterials with ligament width w_0=1 mm in Fig. S2b. The force in the mechanical metamaterial increases with the displacement, while the force in attractive magnets decays rapidly. As the constituent polymer (polyurethane) is elastic, the hysteresis of the metamaterials is also negligible in the quasi-static loading and unloading cycle. The magnets also have negligible hysteresis, as the interactions are free from contact with minimal dissipation. We rescale the measured forces in metamaterials (shown in Fig. S1a) to half, equivalent to one representative unit's cross-section area, and are compared with the magnetic domains in Fig S2b.

In Fig. S2c, we replot the force-displacement curves in logarithmic scales. The force between magnets (F_m) is parameterized with displacement (ΔL) as $F_m=G_m\Delta L^{-4}$, where G_m=340 Nmm^4 for our experiments. The forces in the mechanical metamaterials increase with displacements, $F_s\sim\Delta L^{\xi}$, requiring $\xi\sim1$. The exponent ξ changes slightly with the pore shape aspect ratio, a_0/b_0, as shown in Fig. S2c. The mechanical metamaterials and the magnets respond to the external loading at two distinct length scales, yet their deformation is affined due to the constraint. Therefore, the applied strain/stress, pore geometry, and magnetic interactions dictate the specific transition.

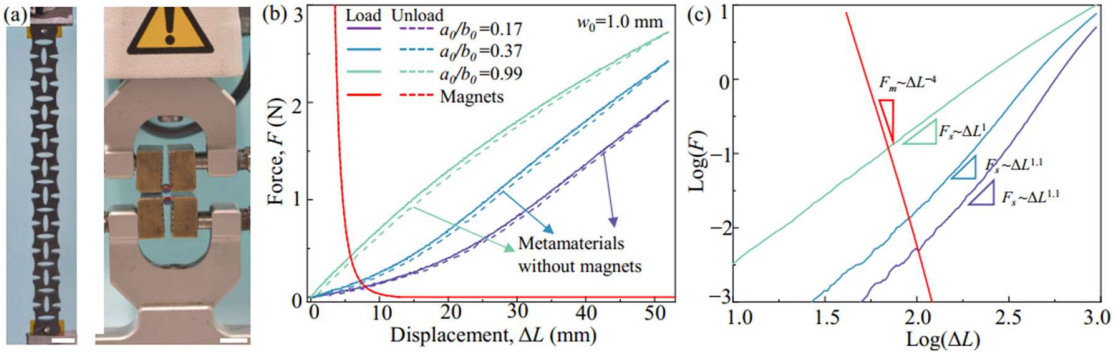

Figure S2. Quasi-static uniaxial tensile experiments in the mechanical metamaterials and attractive magnets. (a) Experimental setup to measure force-displacement curves in metamaterials and magnets. Scale bar, 10 mm. (b) The forces in the attractive magnets and mechanical metamaterials at different displacements. (c) The logarithmic relation between the force and the displacement.

We define the nominal stress in the metamaterial as $\sigma=F/L_0h$. The metamaterials are stretched to the same deformed length before unloading. The displacements in the metamaterials are recorded with a high-resolution camera (Fujifilm X-A10) at a frame rate of 24 fps in the quasi-static experiments. The positions of the 20 markers are placed uniformly along the stretching direction. The positions of the marker are determined via a video analysis software, Tracker (3). We measure local deformation through the positions of the markers, and characterize both the applied global strain, ε_g, and the local strain for the ith magnets, ε_i, as

$$\varepsilon_g=\frac{y_n-y_1}{(n-1)L_0}-1,\varepsilon_i=\frac{y_i-y_{i-1}}{Y_i-Y_{i-1}}-1, \tag{S1}$$

where y_i and Y_i are the positions of the center of the ith magnet in the deformed and undeformed configuration, L_0 is the unit length of metamaterials without magnets, and n=20 in our experiments. As the metamaterials

shorten (elongate) under attractive (repulsive) interactions, the global strain ε_g can be negative (positive) without external loads.

For elasto-magnetic metamaterials with interacting magnets or steel cylinders, additional measurements are provided in Fig. S3 for different metamaterial geometries and magnetic interactions.

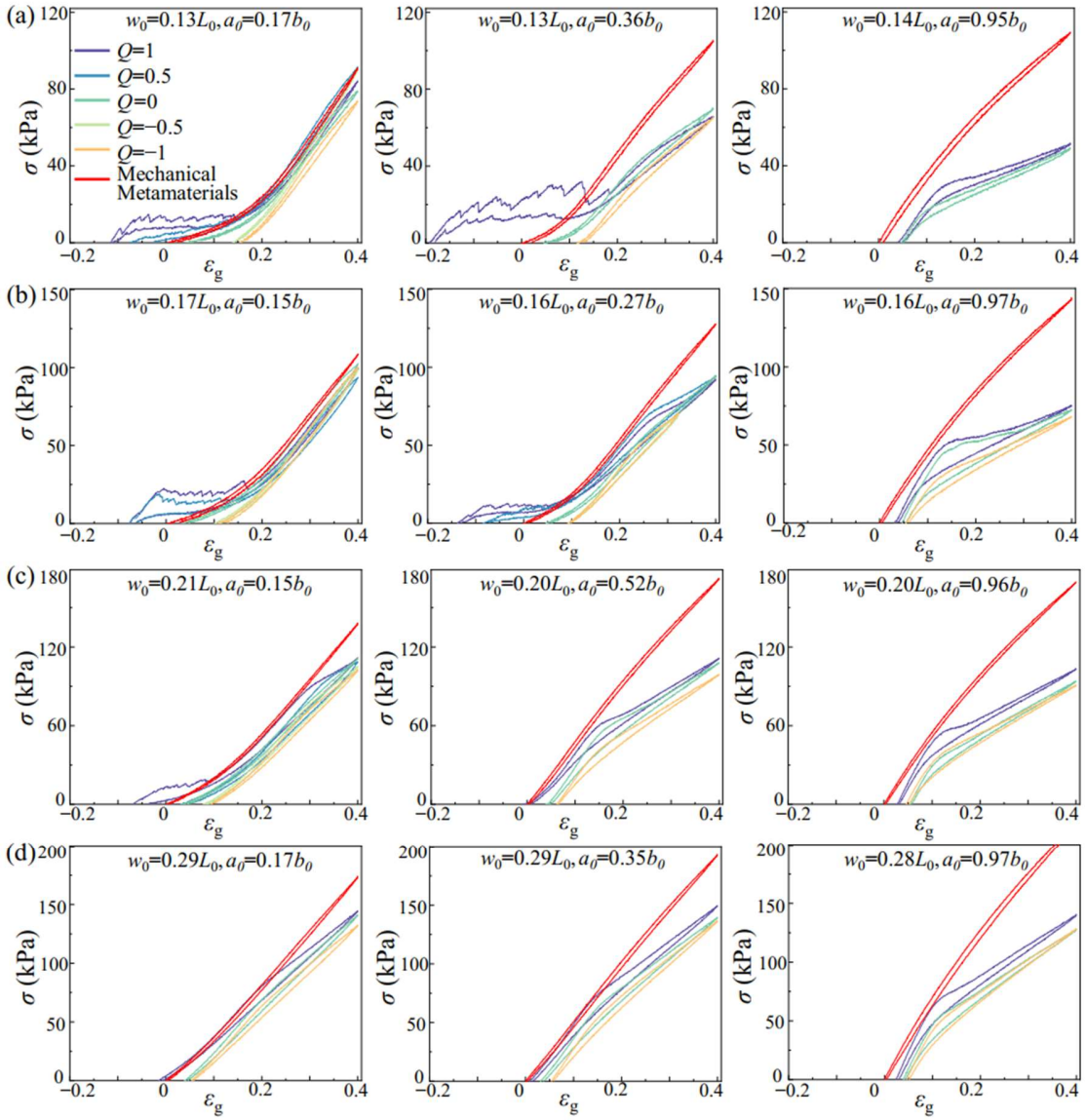

Figure S3. The stress-strain curves of elasto-magnetic metamaterials with different internal structure geometries and magnetic interactions.

We load the samples to the same deformed length for a given global strain for magnetic metamaterials with different internal structures and magnetic interactions. Fig. S4-S7 provides additional experimental results for the metamaterial configurations and local strains in the quasi-static loading and unloading cycle.

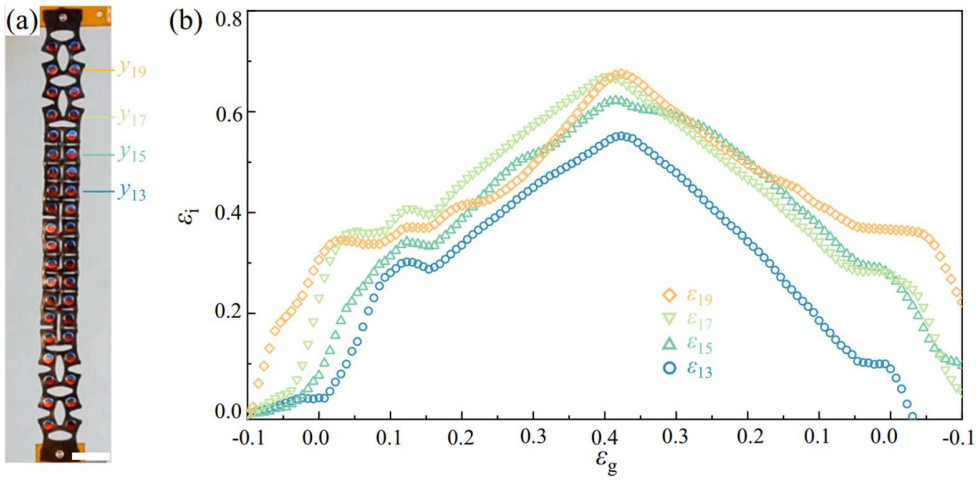

Figure S4. The local strain ε_i, located at the ith magnets in elasto-magnetic metamaterials. (a) Configuration of elasto-magnetic metamaterials with Q=1, w_0=0.13L_0, and a_0=0.17b_0 at a global strain ε_g=0. Scale bar, 10 mm. (b) The local strain ε_i develops with the global strain ε_g in the loading and unloading cycle.

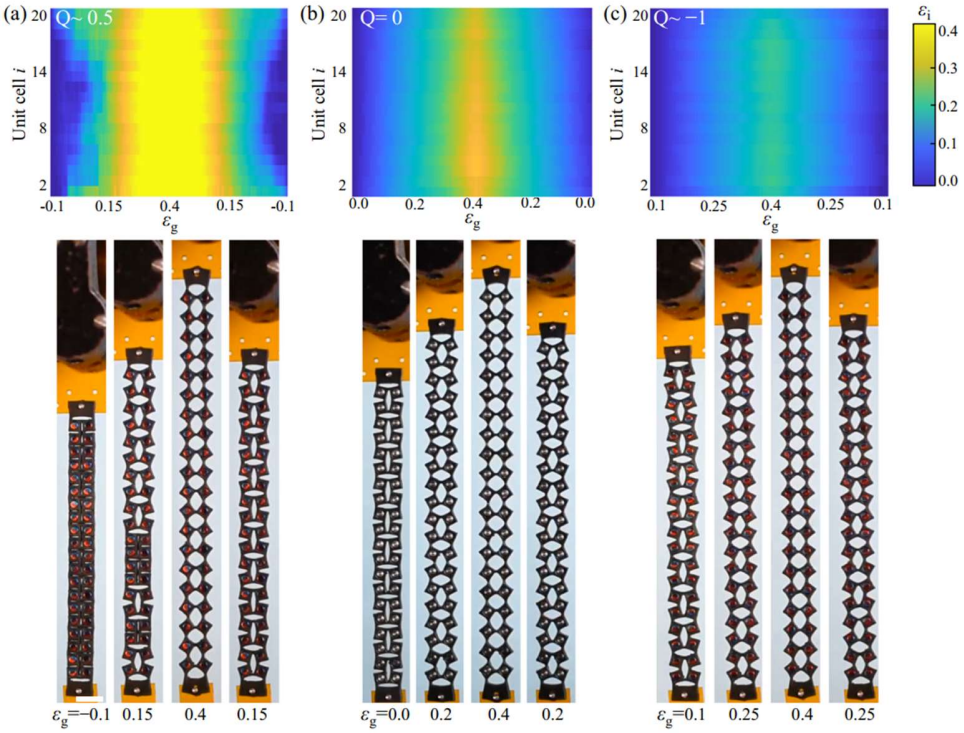

Figure S5. Evolution of the local configurations and local strains of elasto-magnetic metamaterials under external forces. Elasto-magnetic metamaterials are with w_0=0.14L_0 and a_0=0.17b_0. The magnetic interactions range from (a) Q=0.5, (b) Q=0 and (c) Q=−1. Scale bar, 10 mm.

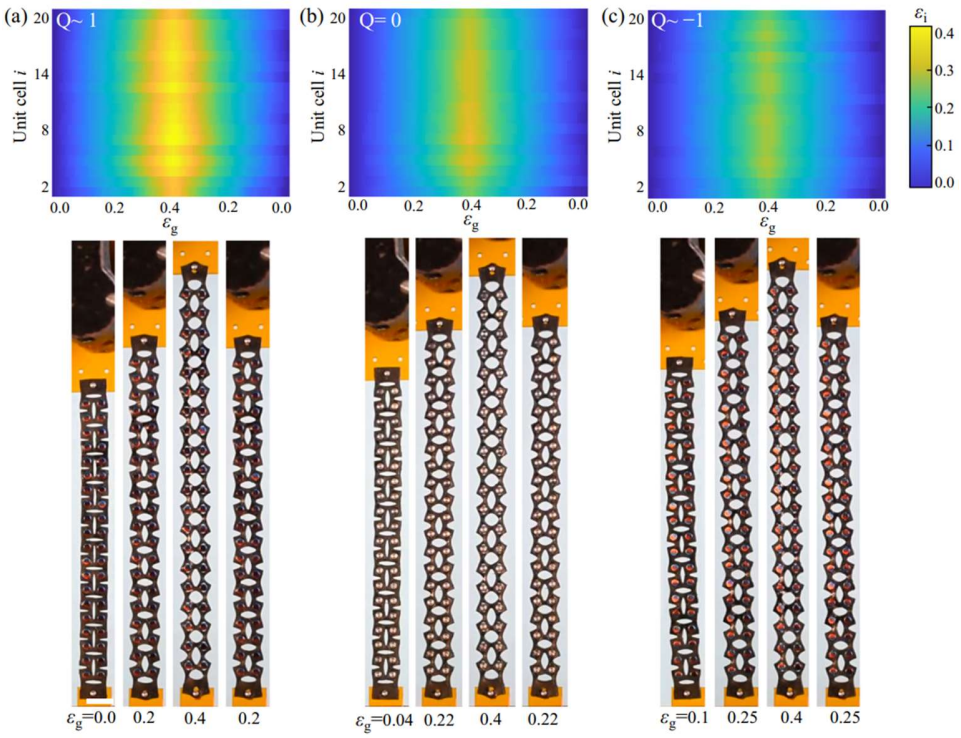

Figure S6. Evolution of the local configurations and local strains of elasto-magnetic metamaterials under external forces. Elasto-magnetic metamaterials are with w_0=0.29L_0 and a_0=0.17b_0. The magnetic interactions range from (a) Q=1, (b) Q=0 and (c) Q=−1. Scale bar, 10 mm.

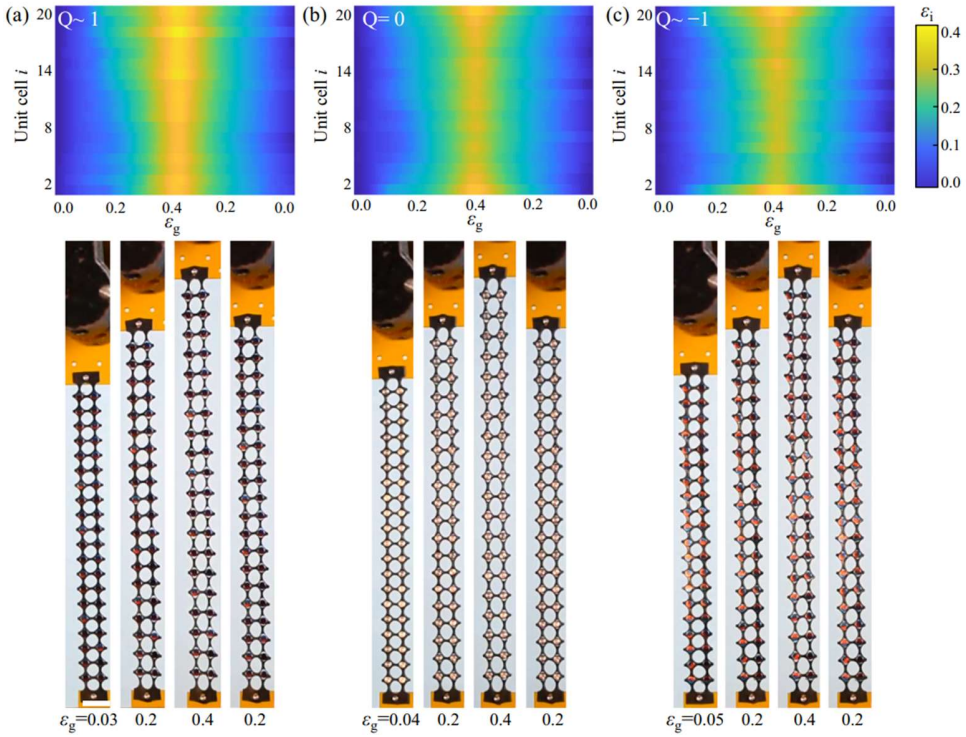

Figure S7. Evolution of the local configurations and local strains of elasto-magnetic metamaterials under external forces. Elasto-magnetic metamaterials are with w_0=0.13L_0 and a_0=0.95b_0. The magnetic interactions range from (a) Q=1, (b) Q=0 and (c) Q=−1. Scale bar, 10 mm.

2.2 High-strain-rate deformation

The high-strain-rate deformation experiments are recorded with a high-speed camera (Photron Fastcam APX RS) at frame rates ranging from 1000 to 10000 fps. A macro zoom lens (Nikon AF Nikkor 24-85 mm) is used to maximize the image with a resolution of 512 × 512, providing a pixel resolution of 400 μm. We mark (Sharpie@ marker, metallic silver) the magnets of metamaterials to track their positions over time from the high-speed videography. The positions of the markers are determined via a video analysis software, Tracker (3). In the tracking, the images of markers before the high-strain-rate deformation are adopted as template images. The evolution rate is set to 20%, allowing for a moderate shape change of the template in deformation. By searching for the best match to the template in each frame, defined with the smallest sum of the square of RGB differences between the template and the match pixels, we obtain the positions of the marker over time.

A. Dynamic recoil

The dynamic recoil tests are performed with the Instron testing machine and a high-speed camera. The metamaterial is positioned at the bottom and top edges through the pins held tightly by pneumatic grips (Fig. S8). The fixation with pins ensures the translational and the rotational displacements are strongly excited in the dynamic recoil. The metamaterial is stretched to a global strain ε_g. The gripper pressure is set to be 70 psi, which is switched off to release the metamaterial to recoil from the bottom edge. Upon release from the grip, the pins move with the recoiling metamaterials (Fig. S8a). The effect of the pin in recoil is minor, as its mass is only 0.8 g, which is much lighter than the metamaterial (11.0 g).

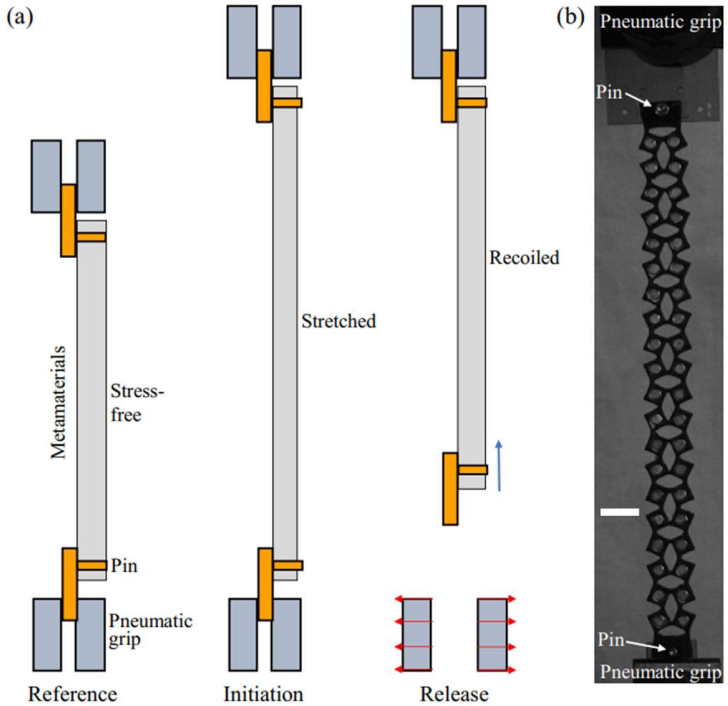

Figure S8. (a) Schematic of the high-strain-rate dynamic recoil in metamaterials. The metamaterial is fixed by the pneumatic grips first, then stretched to a global strain. The dynamic recoil is triggered by releasing the pneumatic grips. (b) The experimental setup for the dynamic recoil. Scale bar, 10 mm.

B. Free-falling mass impact

The impact experiments are performed with a customized free-falling platform in the Instron testing machine (Fig. S9a). The platform is tightly held by pneumatic grips before testing, supporting the mass and the metamaterial. The reference position of the platform is set to make the metamaterial free from external forces. Elastic strings are fixed at the grips and attached to the platform. The strings are stretched as the platform locates at its reference position (Fig. S9b). The mass impact is initiated by switching off the pressure

in the pneumatic grips. The platform moves downwards, driven by the gravitational force and the string retraction force, with an acceleration larger than *g*. The mass losses support from the platform upon release, leading to an impact in the metamaterial with a magnitude determined by its weight.

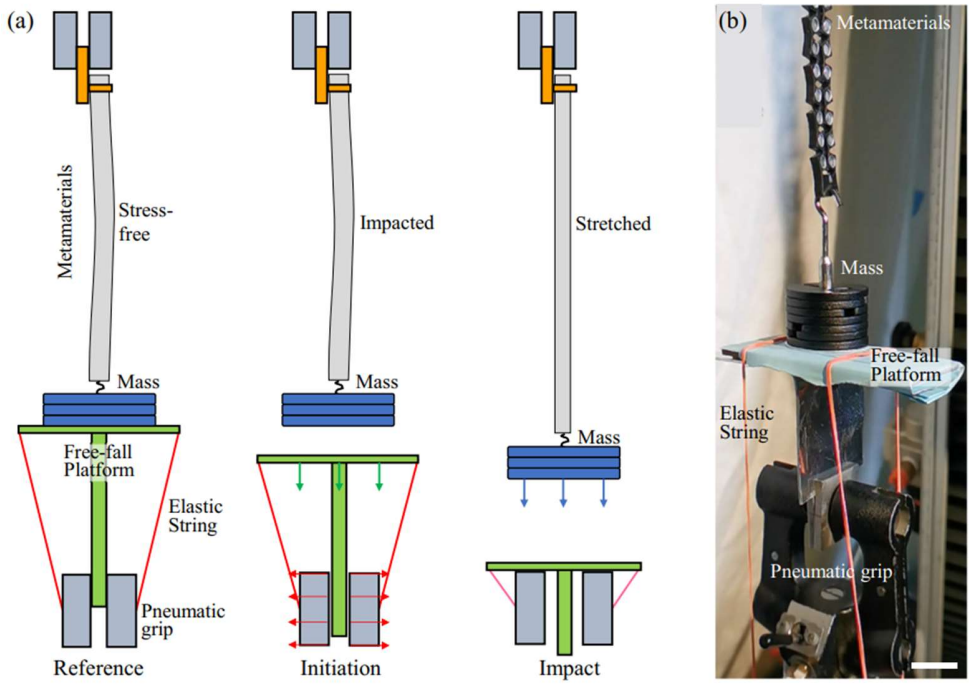

Figure S9. Schematic of the high-strain-rate impact in metamaterials. The metamaterial is connected to a mass with tunable weights. A customized platform held by the pneumatic grip is released to create the free-falling mass impact. (b) The experimental setup for the high-speed impact. Scale bar, 10 mm.

3. Models

We investigate the phase transitions and the corresponding mechanical responses in elasto-magnetic metamaterials analytically. Based on the elastic responses and the magnetic interactions in the metamaterials, we establish an analytical model based on the Landau free energy to qualitatively estimates the phase transitions. Furthermore, the local ligament buckling criterion is developed to predict the design space that permits the formation of the closed phases.

A. Local equilibria of elasto-magnetic metamaterials

Given the mirror symmetry prescribed in the horizontal direction, we use a 1D array of parallel nonlinear springs, representing the elastic and the magnetic interactions (Fig. S10), to predict the local equilibrium conditions. The elastic force in the mechanical metamaterials is described by,

$$F_i^s(u_{i-1}, u_i) = L_0 h \sigma_s(\varepsilon_i), \tag{S2}$$

where $\sigma_s(\varepsilon_i)$ is the nonlinear stress-strain relation of the mechanical metamaterial, $u_{i\text{-}1}$ and u_i denote the axial displacements at two ends of the ith spring. The local strain is $\varepsilon_i=(u_i-u_{i\text{-}1})/L_0=(y_i-y_{i\text{-}1})/(Y_i-Y_{i\text{-}1})-1$, as defined in Eq. (S1). In our analytical model, we assume the magnets behave like perfect magnetic dipoles, the potential energy (V_m) and the force ($\mathbf{F_m}$) between two magnets are (4),

$$V_m(\mathbf{r}) = -\frac{\mu_m}{4\pi|\mathbf{r}|^3}[3(\mathbf{m_1}\cdot\mathbf{r})(\mathbf{m_2}\cdot\mathbf{r}) - \mathbf{m_1}\cdot\mathbf{m_2}], \tag{S3}$$

$$\mathbf{F_m}(\mathbf{r}) = \frac{3\mu_m}{4\pi|\mathbf{r}|^4}\left[(\hat{\mathbf{r}}\times\mathbf{m_1})\times\mathbf{m_2} + (\hat{\mathbf{r}}\times\mathbf{m_2})\times\mathbf{m_1} - 2\hat{\mathbf{r}}(\mathbf{m_1}\cdot\mathbf{m_2}) + 5\hat{\mathbf{r}}\big((\hat{\mathbf{r}}\times\mathbf{m_1})\cdot(\hat{\mathbf{r}}\times\mathbf{m_2})\big)\right], \tag{S4}$$

where μ_m is the magnetic permeability, $\mathbf{m_1}$ and $\mathbf{m_2}$ are the magnetic moments for the neighboring magnets, and $\mathbf{r}$ is the separation vector between the centers of the two magnets, and $\hat{\mathbf{r}}=\mathbf{r}/|\mathbf{r}|$. The separation vector $\mathbf{r}$ is aligned along the vertical direction in our experiments, $|\mathbf{r}|=y_i-y_{i-1}=\delta_0+u_i-u_{i-1}$, and δ_0 is the distance between the center of the neighboring magnets in the closed phase. The magnetic moment also follows $|\mathbf{m_1}|=|\mathbf{m_2}|=m_0$. We can simplify the expression of magnetic potential and the force as,

$$V_i(u_{i-1},u_i)=-\frac{\mu_m}{2\pi r_i^3}(\mathbf{m_1}\cdot\mathbf{m_2}), \tag{S5}$$

$$\mathbf{F_i^m}(u_{i-1},u_i)=\frac{3\mu_m}{4\pi r_i^4}\left[(\mathbf{y}\cdot\mathbf{m_{i-1}})\mathbf{m_i}+(\mathbf{y}\cdot\mathbf{m_i})\mathbf{m_{i-1}}+\mathbf{y}(\mathbf{m_{i-1}}\cdot\mathbf{m_i})-\mathbf{5y}\big((\mathbf{y}\cdot\mathbf{m_{i-1}})\cdot(\mathbf{y}\cdot\mathbf{m_i})\big)\right], \tag{S6}$$

where $r_i=\delta_0+u_i-u_{i-1}$ is the distance between the centers of two magnets. The magnetic moment orientation is described by the angles between the magnetic moment and the y-axis, θ_i and θ_{i-1}. By considering the magnetic force in the vertical direction (y-axis), the nonlinear magnetic force is,

$$F_i^m(u_{i-1},u_i)=-\frac{3\mu_m m_0^2}{2\pi r_i^4}Q, \tag{S7}$$

where $Q=\cos(\theta_i)\cos(\theta_{i+1})$ is the magnets' orientational parameter, $-1\le Q\le 1$.

For the magnetic metamaterial under quasi-static loading, the equilibrium equation can be derived by balancing the nodal forces from the springs,

$$L_0 h[\sigma_s(\varepsilon_{i+1})-\sigma_s(\varepsilon_i)]-G_m Q[(\delta_0+u_{i+1}-u_i)^{-4}-(\delta_0+u_i-u_{i-1})^{-4}]=0, \tag{S8}$$

where $G_m=\frac{3}{2\pi}\mu_m m_0^2$ is the strength of the magnetic interactions, and G_m=340 Nmm^4 measured from our experiments. This is Eq. (2) shown in the main text.

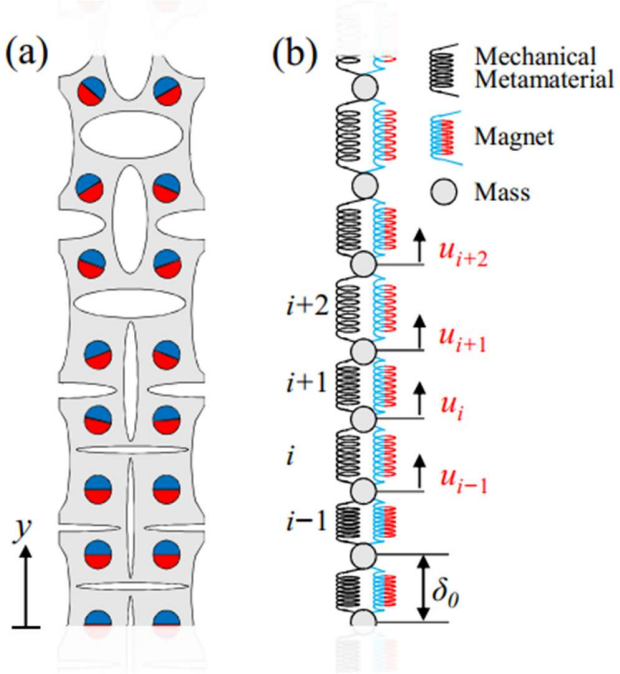

Figure S10. Elasto-magnetic metamaterials' phase transitions and mechanical response are modeled with a 1D array of parallel nonlinear springs. (a) Schematic of elasto-magnetic metamaterials under external forces. (b) The parallel springs between the neighboring masses represent the mechanical metamaterial and the magnets. The center-to-center distance between the neighboring magnets at the closed phase is δ_0. The ith spring displacement is u_i-u_{i-1}, where u_{i-1} and u_i denote the axial displacements at two ends of the spring.

Eq. (S8) describes the local equilibria in the metamaterials under external loadings. Near the phase transitions in the metamaterials, the spring's displacements are small compared to the initial separation, $(u_i-u_{i-1})/\delta_0 \ll 1$. Adopting the anharmonic approximation (5), we can expand the power functions from Eq. (S8) into series to the order of $O((u_{i+1}-u_i)/\delta_0)^2$,

$$\frac{G_m Q}{\delta_0^4}\left(1+\frac{u_{i+1}-u_i}{\delta_0}\right)^{-4} = \frac{G_m Q}{\delta_0^4}\left[1-\frac{4}{\delta_0}(u_{i+1}-u_i)+\frac{10}{\delta_0^2}(u_{i+1}-u_i)^2\right]. \quad \text{(S9)}$$

Combing Eq. (S8) and (S9), we obtain

$$L_0 h[\sigma_s(\varepsilon_{i+1})-\sigma_s(\varepsilon_i)] + \frac{G_m Q}{\delta_0^4}\left[\frac{4}{\delta_0}(u_{i+1}-2u_i+u_{i-1})-\frac{10}{\delta_0^2}(u_{i+1}-2u_i+u_{i-1})(u_{i+1}-u_{i-1})\right] = 0. \quad \text{(S10)}$$

As the metamaterial is represented by a long chain of repeated units (20 in our experiments), the displacement gradients are relatively smooth. We adopt a continuum field, $u(y)$, up to the fourth-order, to describe the discrete displacement, u_i,

$$u_{i\pm1} = u(y \pm L_0) = u \pm L_0\frac{du}{dy} + \frac{L_0^2}{2}\frac{d^2u}{dy^2} \pm \frac{L_0^3}{6}\frac{d^3u}{dy^3} + \frac{L_0^4}{24}\frac{d^4u}{dy^4}. \quad \text{(S11)}$$

In addition, the stress in the mechanical metamaterial $\sigma_s(\varepsilon_i)$ is described as a continuum function of y,

$$\sigma_s(\varepsilon_{i+1}) - \sigma_s(\varepsilon_i) = L_0\frac{d\sigma}{dy}. \quad \text{(S12)}$$

Combining Eq. (S10) – (S12), the continuum limit of the local equilibrium condition is,

$$\frac{d\sigma_s}{dy} + \frac{4G_m Q}{h\delta_0^5}\left(\frac{d^2u}{dy^2}+\frac{L_0^2}{12}\frac{d^4u}{dy^4}\right) - \frac{20L_0 G_m Q}{h\delta_0^6}\frac{du}{dy}\frac{d^2u}{dy^2} = 0. \quad \text{(S13)}$$

The continuous limit of local strain (ε_i) can be expressed as a coarse-grained continuum field $\varepsilon(y)=du/dy$. We trade the detailed trace of the "microscopic" degree of freedom, e.g., u_i, to a coarse-grained continuum field, ε, in the "macroscopic" scale, which is adopted as the order parameter later in the Landau free energy analysis. By integrating Eq. (S13) for y,

$$\sigma_s(\varepsilon) + \alpha_m\varepsilon_{,yy} + k_m\varepsilon - \frac{1}{2}\beta_m\varepsilon^2 = C_0, \quad \text{(S14)}$$

where $\varepsilon_{,yy}=d^2\varepsilon/dy^2$ is the second derivative of ε to y; C_0 is an integration constant. Here $\alpha_m = L_0^2\, G_m Q/3h\delta_0^5$, $k_m = 4\, G_m Q/h\delta_0^5$, and $\beta_m = 20L_0\, G_m Q/h\delta_0^6$, as defined in the main text. Consider that at $y \to \infty$, the metamaterial is stretched to the open phase. The force generated by the magnetic interaction is negligible, and the external force f_p is balanced by force in the mechanical metamaterial. We can find the constant,

$$C_0 = f_p, \quad \text{(S15)}$$

B. Landau free energy of elasto-magnetic metamaterials

Following Landau's analysis in phase transitions (6), we construct a Landau free energy F_L, which is the effective Hamiltonian of the magnetic metamaterial. We use the local equilibrium equation (Eq. (S14)) to obtain the Hamiltonian function under the external force f_p. Based on the Euler-Lagrange theorem, the mechanical equilibrium equation of the magnetic metamaterial follows,

$$\frac{\partial}{\partial y}\left(\frac{\partial L}{\partial \varepsilon_{,y}}\right) - \frac{\partial L}{\partial \varepsilon} = 0, \quad \text{(S16)}$$

where $L(\varepsilon, \varepsilon_{,y})$ is the Lagrangian of the metamaterial and $\varepsilon_{,y}=d\varepsilon/dy$ is the first derivative of ε to y. Combining Eq. (S14) – (S16), the Lagrangian of the magnetic metamaterial can be written as,

$$L(\varepsilon, \varepsilon_{,y}) = \frac{1}{2}\alpha_m(\varepsilon_{,y})^2 - \frac{1}{2}k_m\varepsilon^2 + \frac{1}{6}\beta_m\varepsilon^3 + f_p\varepsilon - \int_0^{\varepsilon}\sigma_s(\gamma)d\gamma\,. \quad \text{(S17)}$$

The Hamiltonian $H(\varepsilon, \varepsilon_{,y})$ is obtained by performing a Legendre transformation on $L(\varepsilon, \varepsilon_{,y})$,

$$H(\varepsilon, \varepsilon_{,y}) = \varepsilon_{,y} \frac{\partial L}{\partial \varepsilon_{,y}} - L. \tag{S18}$$

From Eq. (S17) and (S18), the Hamiltonian of the magnetic metamaterial under the external force f_p is,

$$H(\varepsilon, \varepsilon_{,y}) = \frac{1}{2}\alpha_m(\varepsilon_{,y})^2 + \frac{1}{2}k_m\varepsilon^2 - \frac{1}{6}\beta_m\varepsilon^3 - f_p\varepsilon + \int_0^{\varepsilon} \sigma_s(\gamma)d\gamma\,. \tag{S19}$$

We further neglect the penalty for the strain gradient in the Hamiltonian, $\alpha_m(\varepsilon_{,y})^2/2$, which is always positive and almost zero along the magnetic metamaterial (except for the phase boundaries). The Landau free energy for phase transitions of the magnetic metamaterial under the external force f_p is,

$$F_L(\varepsilon, \varepsilon_{,y}) = -f_p\varepsilon + \frac{1}{2}k_m\varepsilon^2 - \frac{1}{6}\beta_m\varepsilon^3 + \int_0^{\varepsilon} \sigma_s(\gamma)d\gamma\,. \tag{S20}$$

The phase transitions behaviors of elasto-magnetic metamaterials are predicted by the Landau free energy function defined in Eq. (S20). To obtain an analytical prediction of the phase transitions, we approximate the stress-strain relation in the mechanical metamaterial with a polynomial up to third order, $\sigma_s(\varepsilon)=C_1\varepsilon+C_3\varepsilon^3$. Justifications for the polynomial fitting and comparisons with the experiments are provided in Section 4. Substitution of $\sigma_s(\varepsilon)$ to the Landau free energy in Eq. (S20) yields,

$$F_L = -B_1\varepsilon + \frac{1}{2}B_2\varepsilon^2 - \frac{1}{3}B_3\varepsilon^3 + \frac{1}{4}B_4\varepsilon^4, \tag{S21}$$

as defined in Eq. (4) in the main text, $B_1=f_p$, $B_2=(k_m+C_1)$, $B_3=\beta_m/2$, and $B_4=C_3$. We adopt strain ε as an order parameter for the phase transitions in the magnetic metamaterial. The closed and open correspond to the order parameters $\varepsilon\sim0$ and $\varepsilon>0$, respectively. The Landau free energy is obtained near phase transitions as an analytical polynomial function of $\varepsilon\sim0$.

We first compare the well-investigated liquid crystal elastomer system to relate the phase transitions behavior and the Landau free energy. The free energy of the nematic-to-isotropic phase transitions in liquid crystal elastomers can be expanded as powers of the nematic order parameter based on the Landau-de Gennes theory (7),

$$F_L(S, \sigma) = -\frac{\sigma U}{\mu}S + \frac{1}{2}\left(A(T) + \frac{U}{\mu}\right)S^2 - \frac{B}{3}S^3 + \frac{C}{4}S^2, \tag{S22}$$

where S is the order parameter of the liquid crystal molecules, σ is the applied stress, $A(T)$ is a function of the temperature T, B and C are constants, U is the coupling coefficient between mesogenic groups, and μ is the elastic modulus. Due to the nematic symmetry, the Landau expansion of the nematic free energy density contains the odd order powers in Eq. (S22). The liquid crystal elastomer transforms from a nematic phase with orderly aligned molecules ($S>0$) to an isotropic phase with disordered molecules ($S\sim0$) through a discontinuous jump as the temperature increases.

Similarly, elasto-magnetic metamaterials can cross through a closed phase with a small strain ($\varepsilon\sim0$) and an open phase with a finite strain ($\varepsilon>0$) due to the elastic and magnetic interactions. We expect the closed-to-open phase transitions echoes the nematic-to-isotropic phase transitions in liquid crystal elastomer, given the similarity between their Landau free energy density in Eq. (S21) and (S22).

The thermodynamic equilibrium of the phase transitions is achieved at a local minimum of the Landau free energy. For the magnetic metamaterial under external force f_p, the equilibria of different phases follow $\partial F_L/\partial\varepsilon=0$. We also calculate the mechanical critical points as the Landau free energy has merged its maxima and minima (8), satisfying $F_L'(\varepsilon) = F_L''(\varepsilon) = F_L'''(\varepsilon)=0$,

$$\frac{\partial F_L(\varepsilon)}{\partial \varepsilon} = -f_p + B_2\varepsilon - B_3\varepsilon^2 + B_4\varepsilon^3 = 0, \tag{S23}$$

$$\frac{\partial^2 F_L(\varepsilon)}{\partial \varepsilon^2} = B_2 - 2B_3\varepsilon + 3B_4\varepsilon^2 = 0, \tag{S24}$$

$$\frac{\partial^3 F_L(\varepsilon)}{\partial \varepsilon^3} = -2B_3 + 6B_4\varepsilon = 0. \tag{S25}$$

From Eq. (S25), we obtain the critical strain $\varepsilon_{cp}=B_3/3B_4$. Putting ε_{cp} into Eq. (S24) yields $B_2^{cp} = B_3^2/3B_4$, which gives rise to the critical values for the magnetic and elastic interactions in the phase transition. Substituting the critical values ε_{cp} and B_2^{cp} to Eq. (S23) gives $B_1^{cp} = \sigma_{cp} = B_3^3/27B_4^2$. Rescaling the equilibrium equation (Eq. (S23)) with the critical coefficient values from Eq. (S23) – (S25),

$$-\frac{f_p}{\sigma_{cp}} + 3\frac{B_2}{B_2^{cp}}\frac{\varepsilon}{\varepsilon_{cp}} - 3\left(\frac{\varepsilon}{\varepsilon_{cp}}\right)^2 + \left(\frac{\varepsilon}{\varepsilon_{cp}}\right)^3 = 0. \tag{S26}$$

Eq. (S26) is a cubic equation of the strain ε. The scaled external force (f_p/σ_{cp}) and the scaled magnetic and elastic interactions (B_2/B_2^{cp}) govern the phase transitions – from the closed phase with ε~0 to the open phase with finite ε>0.

In the absence of an external force (f_p=0), the Landau free energy is schematically shown in the inset of Fig. 3b in the main text. One solution of Eq. (S26) always exists at ε=0, an extremum of the free energy with $F_L(\varepsilon=0)$=0. Another phase of the magnetic metamaterial (with ε_m>0) appears as the equations $F_L(\varepsilon_m)$=0 and $\partial F_L(\varepsilon_m)/\partial\varepsilon$=0 are satisfied. Combining these two conditions with Eq. (S21) and (S23), we have

$$\frac{\varepsilon_m}{4}\frac{\partial F_L(\varepsilon_m)}{\partial \varepsilon} - F_L(\varepsilon_m) = 0. \tag{S27}$$

To satisfy Eq. (S27), the order parameter at the phase transitions point requires $\varepsilon_m=3B_2/B_3$, leading to a discontinuous jump from the state ε=0 when no external force is applied. Substituting ε_m into $F_L(\varepsilon_m)$=0, it yields,

$$B_2^T = 2B_3^2/9B_4 = \frac{2}{3}B_2^{cp}, \tag{S28}$$

where B_2^T is defined where the two minima of the Landau free energy have an equal depth without external forces. As for $B_2>B_2^T$, the closed phase with ε=0 is the global minimum of the Landau free energy. For $B_2<B_2^T$, the absolute minimum jumps discontinuously from ε=0 to ε_m>0 through first-order phase transitions.

The external force, which contributes as $-f_p\varepsilon$ to the free energy, can modify the phase transitions behavior in the magnetic metamaterial. In Fig. S11, we show the Landau free energy as a function of the scaled order parameter $\varepsilon/\varepsilon_{cp}$ for different magnetic and elastic interactions (B_2/B_2^T) with external forces ranging from $0.5\sigma_{cp}$ to $1.5\sigma_{cp}$. The Landau free energy is scaled as $\bar{F}_L = F_L/(27\sigma_{cp}\varepsilon_{cp})$. The linear term by the external force shifts the minima of the Landau free energy at ε=0 and ε_m=$3B_2/B_3$ to higher values. The critical magnetic and elastic interactions, at which the Landau free energy jumps between two minima, also switch to higher values with increasing external forces.

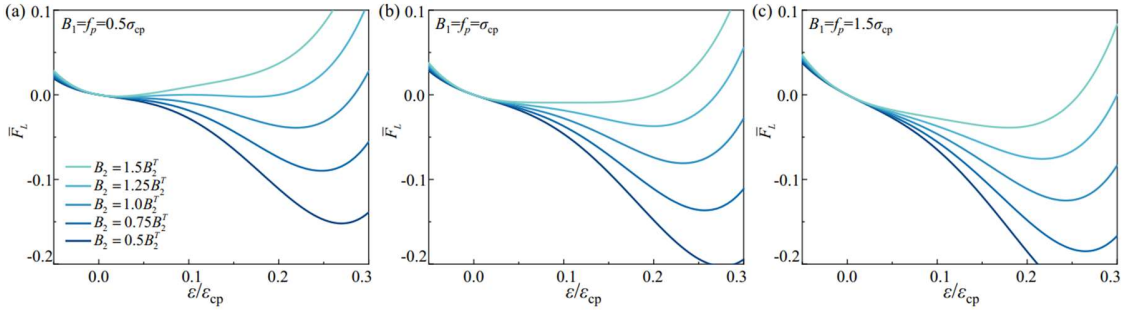

Figure S11. The Landau free energy density plotted against the scaled strain for different magnetic and elastic interactions. The external forces applied to the metamaterial are (a) $0.5\sigma_{cp}$, (b) σ_{cp}, and (c) $1.5\sigma_{cp}$.

The dependence of the phase transitions behaviors upon the external forces and the magnetic and elastic interactions is obtained by solving Eq. (S26) numerically. In Fig. S12a, we plot the scaled order parameter $\varepsilon/\varepsilon_{cp}$ against the scaled magnetic and elastic interactions B_2/B_2^T in the presence of external forces f_p. Each point in the curve is a local minimum of the Landau free energy, representing the equilibrium state for a

phase in the metamaterial. However, some of the equilibria states are only metastable since it has higher free energy. To obtain the analytical expression of the critical conditions, we seek a solution of the order parameter ε in a form (7, 8),

$$\varepsilon_{\pm} = \varepsilon_{cp}\left(1 \pm \sqrt{3-\tau}\right), \tag{S29}$$

where $\varepsilon_{\pm}$ is the critical strains for the coexisting phases; τ is to be determined and depends on the external forces and the magnetic and elastic interactions. Inserting Eq. (S29) into Eq. (S26), it yields,

$$\frac{2B_2^{\pm}}{B_2^T} = \left(\frac{f_p}{\sigma_{cp}}\frac{1}{\tau-2} - 1\right)\left(1 \pm \sqrt{3-\tau}\right) + \tau, \tag{S30}$$

where $B_2^{\pm}$ is the critical magnetic and elastic interactions for the coexisting phases. Eq. (S30) is valid for all values of τ, indicating that the term with $\sqrt{3-\tau}$ should vanish,

$$\tau = \frac{2B_2^{\pm}}{B_2^T}, \tag{S31}$$

$$\frac{f_p}{\sigma_{cp}} = \tau - 2. \tag{S32}$$

Therefore, the critical strains and the critical magnetic and elastic interactions for the phase transitions in the presence of the external force are,

$$\varepsilon_{\pm} = \varepsilon_{cp}\left(1 \pm \sqrt{1 - \frac{f_p}{\sigma_{cp}}}\right), \tag{S33}$$

$$\frac{B_2^{\pm}}{B_2^T} = 1 + \frac{1}{2}\frac{f_p}{\sigma_{cp}}. \tag{S34}$$

In Fig. S12b, we plot ε_+, ε_- and $B_2^{\pm}$ as a function of the scaled external force f_p/σ_{cp}. As for a small external force ($f_p<\sigma_{cp}$), the phase transitions are first-order and changes discontinuously between the strains ε_+ and ε_- in the closed and open phases. As the external force increases beyond the critical stress σ_{cp}, the metamaterials do not have discontinuities in the order parameter ε at any magnetic and elastic interactions. The closed-to-open phase transformation is of second-order when $f_p=\sigma_{cp}$, with $\varepsilon_+=\varepsilon_-=\varepsilon_{cp}$. Combining the local minima for the Landau free energy with the critical condition for the phase coexistence in Fig. S12, we construct phase transitions for the magnetic metamaterial, as shown in Fig. 3b in the main text.

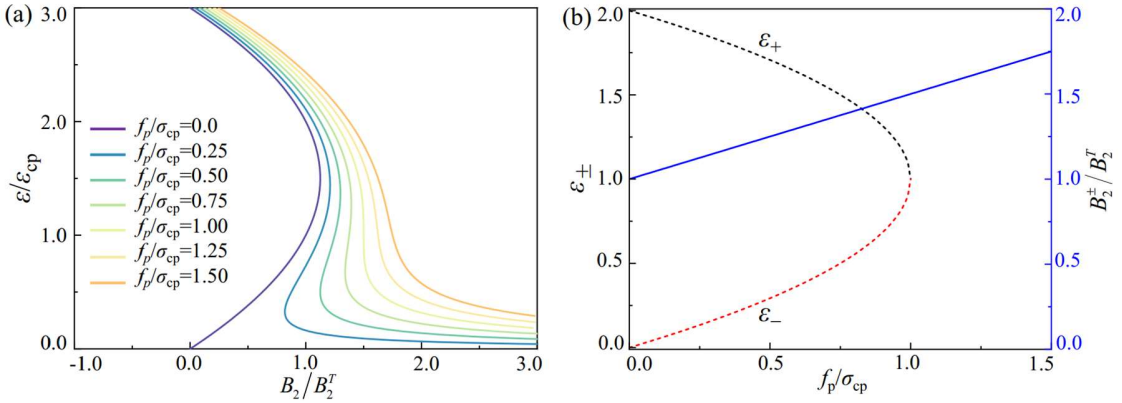

Figure S12. (a) The order parameter against the magnetic and elastic interactions for the local minima of the Landau free energy with different external forces. (b) The critical strains (dashed lines) for the coexisting phases and the critical magnetic and elastic interactions (solid line) for the phase transitions.

C. Ligament buckling

The bending stiffness of the ligament connecting the neighboring magnets depends on the internal structure geometry (1). Upon uniaxial compression, the bending stiffness increases as the pore aspect ratio (a_0/b_0) increases, changing from a compliant hinge to a stiff slender bar (1). As shown in Fig. S13a, we derived the ligament's bending stiffness by mapping it onto a pre-curved beam (2). The neutral axis of the beams is curved with a non-constant cross-section, and the bending stiffness of the ligament is,

$$C_b = \frac{8\sqrt{2}\mu_0 h}{3\pi(1-a_r)^2} a_0^2 w_0^{\frac{5}{2}} (L_0 - w_0)^{-\frac{1}{2}} \left(L_0^2 + \frac{2}{3} w_0 (L_0 - w_0) \right)^{-1}, \tag{S35}$$

where μ_0 is the shear modulus of the polymer in the ligament, μ_0=0.56 MPa; a_r=a_0/b_0 is the metamaterial pore aspect ratio. As indicated in Eq. (S35), the ligament's bending stiffness C_b grows as a_r increases, making the bending difficult in the uniaxial loading. Therefore, a stronger magnetic interaction is required to form a closed phase. Finally, it leads to a ligament buckling instead of bending as the pores become circular.

The ligament in a circular pore pattern under compressive forces is modeled as a column buckling with pin supports. The critical load for buckling is (9),

$$F_{cr} = \frac{\pi^2 C_b L_0}{L^2}, \tag{S36}$$

where C_bL_0 is the bending rigidity of the ligament, L is the length between the two pin supports, L=L_0. The force generated by magnetic interactions is F_m=G_mQ/L_0^4 (Fig. S11b). The closed phase can be found as the ligament buckles between the magnets and the pores collapse with F_m=F_{cr}, requiring

$$Q_b = \frac{8\sqrt{2}\pi}{3} \bar{G}_m^{-1} \frac{a_r^2}{(1-a_r^2)^2} \bar{w}_0^{\frac{5}{2}} (1-\bar{w}_0)^{\frac{3}{2}} \left(1 + \frac{2}{3} \bar{w}_0 (1-\bar{w}_0) \right)^{-1}, \tag{S37}$$

where $\bar{G}_m = G_m/(\mu_0 h L_0^5)$ is the scaled magnetic strength and $\bar{w}_0 = w_0/L_0$ is the scaled ligament width.

We adopt the scaled magnetic strength $G_m/(\mu_0 h L_0^5) = 0.025$, based on independent measurements in our material system. The buckled magnetic orientation (Q_b) represents the smallest orientation values to induce buckling in metamaterials for a given metamaterial. In Fig. S13c, we plot the contour lines for the critical metamaterial geometries for different fixed values of Q_b, ranging from 0.1 to 1. The geometry parameters a_r and w_0/L_0 lying above the contour lines of Q_b will not buckle under the compressive magnetic forces. For a near-circular pore pattern (a_r~1) and a large ligament width (w_0/L_0 >>0), the ligament always resists buckling regardless of the magnet's orientation (Fig. S13c). As a result, the magnetic metamaterial with such geometry can only support the open phase.

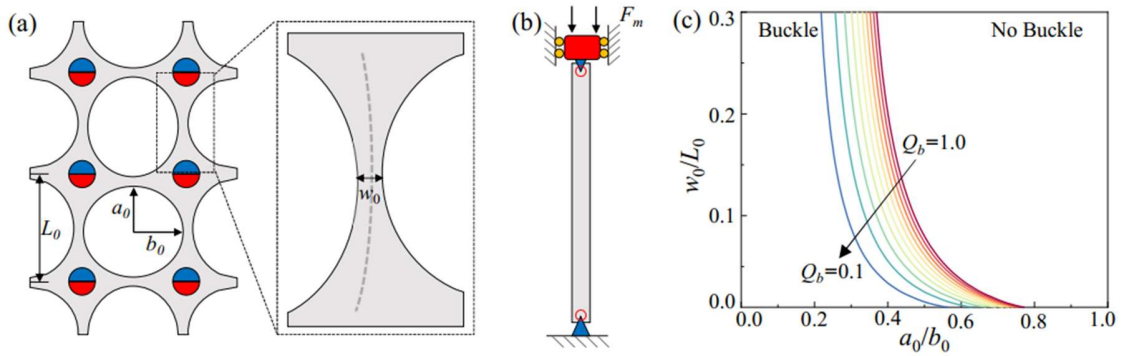

Figure S13. (a) The ligament in metamaterials modeled as a pre-curved beam with a non-constant cross-section. (b) Ligament buckling under the compressive force F_m by the attracting magnets. The ligament is modeled as a simply supported Euler beam with length L_0. (c) The contour lines for the metamaterial geometries required to induce the ligament buckling for different magnet orientations (Q_b=0.1 ~ 1.0).

4. Phase diagram for elasto-magnetic metamaterials

We construct the phase diagram for the magnetic metamaterial based on the Landau free energy and the ligament buckling conditions developed in Section 3. The phase diagram depicts the design space that permits a dual-phase (closed and open phases) and supports a discontinuous phase transitions from a closed to an open phase.

A. Stress-strain relation in mechanical metamaterials

The elastic stress-strain relation in metamaterials is controlled by the metamaterial geometries (Fig. S14a). We have developed an analytical solution for the stress-strain responses in our previous work (1). Instead of adopting the exact analytical expression of the stress, we follow Landau's analysis and approximate the metamaterial's elastic energy with an analytical function of strain ε. In the neighborhood of the phase transitions, where the strain ε is small, we can expand $\sigma_s(\varepsilon)$ in powers of ε,

$$\sigma_s(\varepsilon) = \mu_0 \overline{w}_0 (g_1(a_r)\varepsilon + g_2(a_r)\varepsilon^2 + g_3(a_r)\varepsilon^3). \tag{S38}$$

where $g_1(a_r)$, $g_2(a_r)$, and $g_3(a_r)$ are the fitting functions reflecting the dependence upon the metamaterial geometry. We drop the even order term in σ_s in the main text by assuming the strain energy is symmetric around ε~0 at tension and compression. This assumption is valid for metamaterials with the elliptical pore pattern and will be further verified in this section. Such symmetry is broken in the metamaterial with circular pores as the ligament buckles under the compressive loads. To account for this alternative deformation path, we introduce a ligament buckling criterion to estimate the phase boundary in Section 3. In addition, the dependence upon pore geometry is neglected at the higher-order term of ε for simplicity, with $g_3(a_r)=c_3$ being a measured material constant. The fitting stress-strain relation adopted in the main text is,

$$\sigma_s(\varepsilon) = \mu_0 \overline{w}_0 \big((1.75 + 2a_r)\varepsilon + 4.5\varepsilon^3\big). \tag{S39}$$

Therefore, the stress-strain relation in the mechanical metamaterials adopted in the main text, $\sigma_s(\varepsilon)=C_1\varepsilon+C_3\varepsilon^3$, can be written as $C_1 = (1.75 + 2a_r)\mu_0\overline{w}_0, C_3 = 4.5\mu_0\overline{w}_0$.

In Fig. S14b, we plot the stress-strain relation of the mechanical metamaterial with the polynomial function in Eq. (S39). Albeit simple, the fitting stress-strain relation captures the stress-strain responses in the mechanical metamaterials, especially the dependence upon pore aspect ratio and ligament width. We note that the accuracy can be improved by adding the even order term in σ_s and considering the pore geometry at the higher-order terms. For instance, a more accurate stress-strain relation is obtained by adopting,

$$\sigma_s(\varepsilon) = \mu_0 \overline{w}_0 \big((-0.03 + 6.15a_r)\varepsilon + (5.73 - 13.35a_r)\varepsilon^2 + 4.5\varepsilon^3\big). \tag{S40}$$

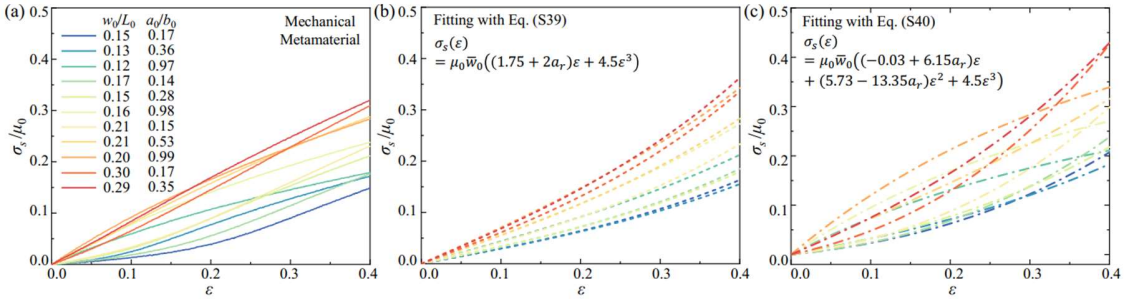

Figure S14. Stress-strain relation in the mechanical metamaterial under uniaxial stretching. (a) The experimental stress-strain responses of mechanical metamaterials with different pore shapes and ligament widths. (b) The stress-strain responses fitted by the polynomial function of $\sigma_s(\varepsilon)=\mu_0\overline{w}_0(g_1(a_r)\varepsilon+c_3\varepsilon^3)$. (c) The stress-strain responses fitted by the polynomial function with the second-order term ε^2, $\sigma_s(\varepsilon)=\mu_0\overline{w}_0(g_1(a_r)\varepsilon+g_2(a_r)\varepsilon^2+c_3\varepsilon^3)$. The expressions of the fitting functions are shown in the inset.

In Fig. S14c, we plot the stress-strain relation of the mechanical metamaterial with Eq. (S40). The addition of the second-order term ε^2 improves the accuracy in describing the strain stiffening and softening responses induced by the pore aspect ratio in the mechanical metamaterials. However, the improvement is purely mathematical without considering the physical mechanisms. For example, the transition between internal

rotational and translational displacement, the competition among the ligament bending, twisting, and stretching deformation, signifying in our previous studies (1), are not yet captured in the fitting function with the addition of the second-order term. The fitting stress-strain relation in Eq. (S40) incorporates the first-order term with parameter $C_1 = (-0.03 + 6.15a_r)\mu_0\bar{w}_0$, which is near zero with small a_r for all metamaterials with elliptical pores, neglecting the effect of ligament bending. More importantly, the additional second-order term ε^2 also violates symmetry of the strain energy between compression and tension around ε~0, which could affect the analysis of the Landau free energy around the critical points in phase transitions. The following section will demonstrate how the additional term in the fitting function modifies predictions of the critical conditions in the Landau free energy analysis.

B. Phase transitions in mechanical metamaterials

We adopt the critical condition for the first-order phase transitions (Eq. (S34)) to predict elasto-magnetic metamaterials' single and dual-phase phase boundaries. The lower bound that permits the existence of a dual-phase and supports discontinuous phase transitions requires,

$$B_2 = B_2^T, \tag{S41}$$

where B_2^T represents the coupling between the magnetic interaction and the mechanical metamaterial constitutive response that permits the first-order phase transitions without external force (f_p=0). By substituting the expression of B_2^T into Eq. (S41), the condition for phase transitions is written as,

$$2B_3^2 - 9B_2B_4 = 0, \tag{S42}$$

which is Eq. (6) in the main text. We can further express the condition with the parameters defined in the magnetic metamaterial. By adopting stress-strain relation in Eq. (S39), which is also adopted in our main text, we can explicitly express,

$$\begin{aligned} B_2 &= \frac{4G_mQ}{h\delta_0^5} + \mu_0(1.75 + 2a_r)\bar{w}_0, \\ B_3 &= \frac{10G_mQL_0}{h\delta_0^6}, \\ B_4 &= 4.5\mu_0\bar{w}_0. \end{aligned} \tag{S43}$$

The condition for phase transitions in Eq. (S42) is rewritten as,

$$\left(\frac{L_0}{\delta_0}\right)^{12}\bar{G}_m^2Q^2 - 0.81\bar{w}_0\left(\frac{L_0}{\delta_0}\right)^5\bar{G}_mQ - 0.2025(1.75 + 2a_r)\bar{w}_0^2 = 0, \tag{S44}$$

where δ_0=4 mm and L_0/δ_0=1.5. The closed phase requires an attractive magnetic interaction Q>0. Therefore, the critical condition for phase transitions in the magnetic metamaterial is,

$$Q_L = 0.405\bar{w}_0\left(\frac{L_0}{\delta_0}\right)^{-7}\bar{G}_m^{-1}\left(1 + \sqrt{1 + (2.16 + 2.47a_r)\left(\frac{L_0}{\delta_0}\right)^2}\right). \tag{S45}$$

The magnetic orientation (Q_L) represents the smallest values that support a dual-phase (closed and open phases) needed for the phase transitions. In Fig. S15a, we plot the contour lines for the critical internal structure geometries needed to support first-order phase transitions, where the elastic responses in the metamaterials is fitted by the stress-strain relation with odd-order terms (Eq. (S39)). The metamaterials geometries supporting phase transitions expand as Q_L increases from 0.1 to 1, as the magnetic domains generate larger attractive forces. For the metamaterials with a_r and w_0/L_0 above the contour lines of Q_L, which indicate a thicker ligament and a circular pore shape, the magnetic metamaterial only supports the open phase.

To identify the effect of the fitting stress-strain relation in the phase transitions in metamaterials, we also predict the contour lines of Q_L with Eq. (S40). The fitting stress-strain relation includes the additional geometric effect in the second-order term ε^2, which captures the softening response in metamaterials with small a_r. By adopting Eq. (S40) in the Landau free energy, we can explicitly express the parameters,

$$B_2 = \frac{4G_m Q}{h\delta_0^5} + \mu_0(-0.03 + 6.15a_r)\bar{w}_0,$$
$$B_3 = \frac{10G_m Q L_0}{h\delta_0^6} + \mu_0(5.73 - 13.35a_r)\bar{w}_0, \quad \text{(S46)}$$
$$B_4 = 4.5\mu_0\bar{w}_0.$$

By substituting Eq. (S46) into Eq. (S42), we determine the contour lines of Q_L for the critical metamaterial geometric conditions for phase transitions in Fig. S15b.

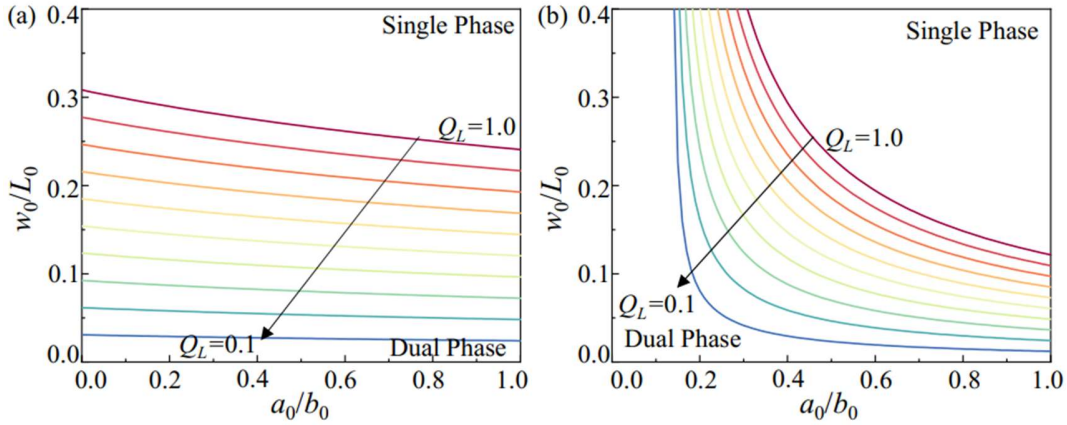

Figure S15. The contour lines for the critical geometries in metamaterials induce phase transitions for different magnet orientations (Q_L=0.1 ~1.0). (a) The contour lines predicted by the stress-strain relation with only the odd-order terms (Eq. (S39)). (b) The contour lines predicted by the stress-strain relation with the additional second-order term (Eq. (S40)).

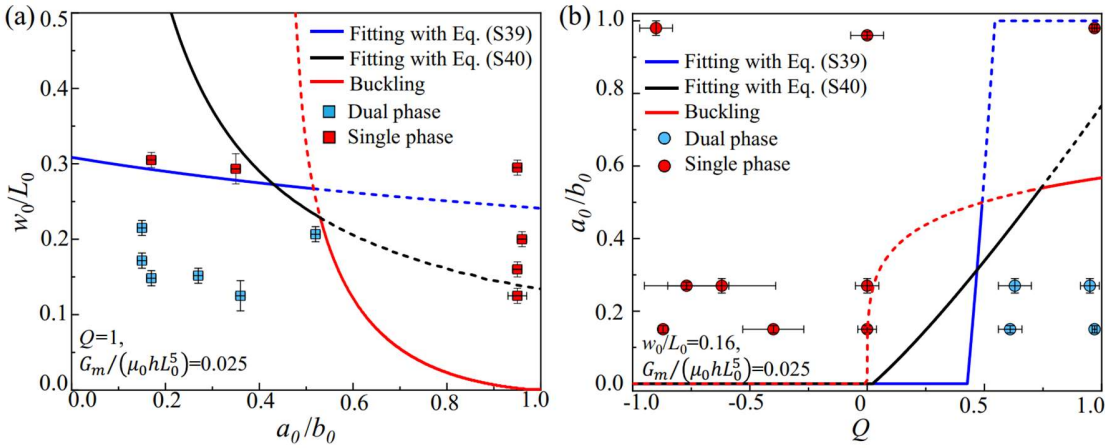

Figure S16. The phase diagram is predicted by two different elastic stress-strain relations for a fixed magnetic moment direction (Q=1) in (a) and a fixed ligament width (w_0/L_0=0.16) in (b). The experimental observations of the single and the dual-phase metamaterials are shown with symbols. The predictions from the ligament buckling analysis are plotted with red lines.

The additional second-order term in Eq. (S40) captures the softening and stiffening elastic responses in the mechanical metamaterials. As shown in Fig. S15b, the critical ligament width supporting the single phase decreases as a_r approaches 1, while it quickly increases as a_r approaches 0. The changes in the Landau free energy analysis predictions are due to the modification in the parameters B_2 in Eq. (S46). The stiffening effect in the metamaterials with circular pores (a_r ~1) is captured with the fitting functions with the second-order term. However, modifying the fitting stress-strain relation also substantially reduces the elastic effect of the

ligament width in the B_2 term in the Landau free energy (Eq. (S46)) as a_r approaches 0. This is because the competition between the elastic and magnetic interactions is absent for the metamaterial with elliptical pores. Therefore, unphysical predictions of the elasto-magnetic metamaterials with elliptical pores, which always supports a closed-to-open phase transition regardless of the ligament width, is resulted from the fitting stress-strain relation with the second-order term.

Finally, we compare the phase diagram predicted by two different stress-strain relations and experimental observations for a fixed magnetic moment direction (Q=1) and a fixed ligament width (w_0/L_0=0.16) in Fig. S16. Similar to the one presented in Fig. 3c and 3d in the main text, the boundaries separating the single and dual phases are similar regardless of the fitting functions for the elastic responses. For the fixed attractive magnetic interaction in Fig. S16a, the stress-strain relation with the additional second-order term in Eq. (S40) predicts the phase boundary with a smaller ligament width as a_r approaches 1, while overestimating the ligament width that supports a closed-to-open phase transition as a_r is small. For the fixed ligament width in Fig. S16b, adding the second-order term in the stress-strain relation smoothens the transition in phase boundary as magnetic interactions change from repulsive to attractive. However, the transition domain is mostly governed by the ligament buckling criterion, which is already captured in our model without adding the second-order term in the stress-strain relation.

The improvement by incorporating the second-order term in the stress-strain relation is purely mathematical while sacrificing the inherent symmetry in the strain energy between compression and tension in mechanical responses. Therefore, we predict the phase diagram with the stress-strain relation with the odd-order terms in Eq. (S39) and the buckling criterion in the main text.

C. Determining the closed-to-open phase transition in experiments

We predict the phase diagram for the elasto-magnetic metamaterials with the Landau free energy in Section 3B. As shown in Fig. 3b and Fig. S12, the scaled strains $\varepsilon/\varepsilon_{\mathrm{cp}}$ are plotted as a function of B_2/B_2^T, which is the reduced parameter for the coupling between the magnetic interaction and the elastic constitutive response, with different external forces f_p/σ_{cp}. In this section, we demonstrate how we interpret the experimental data for metamaterials that experience a closed-to-open phase transition in Fig. 2a into the phase diagram in Fig. 3b.

The elasto-magnetic metamaterials with elliptical pore patterns (w_0=0.17L_0 and a_0=0.17b_0) experience a closed-to-open phase transition with attractive magnetic domains (Q=0.98). The critical values are $\varepsilon_{cp}=B_3/3B_4$. and $B_2^T = 2B_3^2/9B_4$, where the expressions for B_3 and B_4 are provided in Eq. (S43). We adopt the strength of the magnetic interaction G_m=340 Nmm^4 and the shear modulus of the polymer μ_0=0.56 MPa from independent measurements. The thickness and the size of the unit cell in the metamaterials are h=3.2 mm and L_0=6 mm, respectively. Given the phase transitions in the elasto-magnetic metamaterials initiates at a finite strain (~0.06) as shown in Fig. 2a, different values of the distance between magnets, δ_0, are taken for the calculations. The critical values ε_{cp} and B_2^T are predicted based on the undeformed configuration, where δ_0=0.75L_0, while the values B_2 are predicted as the discontinuous phase transitions happen, with δ_0=0.95L_0. The strains for the coexisting phase $\varepsilon_{\pm}$ (the starting and ending points of the plateau in the stress-strain curve) are ε_{-}~0.06 and ε_{+}~0.238. Therefore, we can interpret the experimental data for the metamaterials in Fig. 2a into Fig. 3b, with $\varepsilon_{-}/\varepsilon_{\mathrm{cp}}$~0.312, $\varepsilon_{+}/\varepsilon_{\mathrm{cp}}$~1.547 and B_2/B_2^T=1.29, which are marked with solid circles in Fig. 3b in the main text.

5. High-strain-rate deformation

We demonstrate the new capacities enabled by phase transitions in elasto-magnetic metamaterials, significantly enhancing dynamic performances in high-strain-rate deformation. A sequential dynamic recoil due to the elastic and the magnetic coupling is observed, which supports the propagation of nonlinear waves and programs the dynamic recoil velocity. Furthermore, the shift from a closed to an open phase dissipates a

large amount of energy, modulating the energy dissipation when the metamaterials are subjected to an impact loading.

A. Dynamic Recoil

The high-strain-rate recoil experiments are conducted in metamaterials (w_0=1 mm and a_0=0.17b_0) with different magnetic interactions (Q=1, 0, and −1). The positions corresponding to the color markers in Fig. 4a are plotted against the recoil time in Fig. S17. The metamaterials recoil with a constant recoil velocity V_R, which is the maximum slope of the measured displacement-time curves. The metamaterials with Q=0 (Fig. S17b), in which the recoil velocity is controlled by the elastic response alone, recoil in a velocity of about 1.2 m/s. The attractive magnetic interaction with Q=1 in elasto-magnetic metamaterials (Fig. S17a) increases the recoil velocity, reaching around 1.8 m/s. The recoil velocity drops to 0.8 m/s as the interaction becomes repulsive with Q=−1 (Fig. S17c). The recoil is self-similar at different locations in metamaterials with different magnetic interactions, indicating that the material/structural damping for the dynamic recoil is weak. Thus, the magnetic interaction is the primary cause for the variations in recoil velocity.

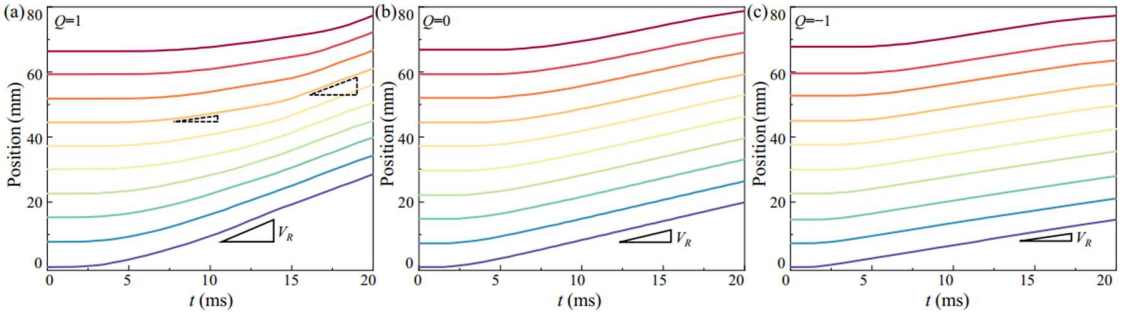

Figure S17. The metamaterials' positions with the elliptical pore pattern (w_0=1 mm and a_0=0.17b_0) measured against the recoil time. The magnetic interactions range from attractive with Q=1 in (a), neutral with Q=0 in (b), and repulsive with Q=−1 in (c). The recoil velocity V_R is the maximum slope for the displacement-time curves.

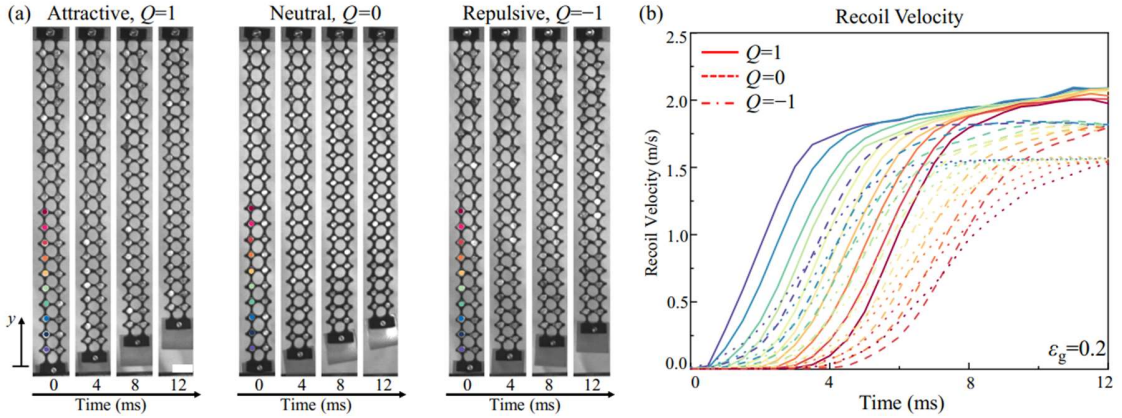

Figure S18. Elasto-magnetic metamaterials with the circular pore pattern (w_0=1 mm and a_0=0.97b_0) in dynamic recoil. (a) High-speed images of elastic recoil in metamaterials with different magnetic interactions. (b) Recoil velocity in metamaterials corresponding to the color markers in (a) over time.

We also notice a sequential dynamic recoil observed in metamaterials with attractive magnetic interaction (Q=1). The metamaterials recoil with a smaller velocity before reaching the maximum V_R (Fig. 4b), marked by the dashed lines with different slopes in Fig. S17a. The sequential dynamic recoil is due to the elastic and magnetic responses (Fig. S2b). The metamaterials recoil with a smaller velocity at a larger strain, governed

by elastic recoil of the ligament. As the attractive magnetic domains approach each other in recoil, the phase transitions, from the open to closed phase, propagate as a nonlinear wave, increasing the recoil velocity.

We further demonstrate that the propagation of the phase transitions instead of the attractive magnetic force modulates the dynamic recoil by performing recoil experiments in metamaterials with circular pores (Fig. S18). By stretching the metamaterials to the same deformed length with ε_g=0.2, we tracked the positions of the metamaterials in dynamic recoil with different magnetic interactions (Q=1, 0, and −1). The metamaterials (w_0=1 mm and a_0=0.97b_0) only support a single open phase for all magnetic interactions (Fig. S18a). Unlike the metamaterials supporting the phase transitions (Fig. 4a), the dynamic recoil in the metamaterials with circular pores is manifested by translational retraction of the ligaments (Fig. S18a) without transforming the phases. As shown in Fig. S18b, the recoil velocity varies less than 10% in metamaterials with magnetic interactions (attractive or repulsive) compared to the elastic recoil with Q=0. Therefore, the propagation of the phase transitions is critical to program the dynamic recoil in elasto-magnetic metamaterials.

B. Damping in impact oscillations

In the main text, we show the impact experiments in metamaterials with the elliptical pore pattern (w_0=1 mm and a_0=0.17b_0). The free-falling mass impact in metamaterials without the magnetic interaction (Q=0) is shown in Fig. S19, which results in a damped harmonic oscillation. The impact energy is dissipated as frictions in the internal structures and viscoelastic responses of the material. The dissipative force due to the viscous damping is proportional to velocity (10). We model the vibration as a simple single degree of freedom system consisting of only a spring, a dashpot, and a mass. The equation of motion is,

$$m\frac{d^2y}{dt^2} = -ky - \eta\frac{dy}{dt}, \tag{S47}$$

where m is the mass; k is the stiffness of the metamaterial; η is the damping constant. The solution for the damped harmonic oscillation, the position of the mass can be expressed as,

$$y(t) = A_0\left(1 + e^{-\frac{t}{\tau_0}}\cos\left(\frac{2\pi t}{T_0} + \phi\right)\right), \tag{S48}$$

where τ_0=2m/η is the decay time; $T_0 = 2\pi/\sqrt{k/m - \eta^2/4m^2}$ is the period of oscillations; A_0 is the amplitude, proportional to the impact mass weight; ϕ is the phase constant determined by the initial and boundary conditions. As shown in Fig. S19a, the damped oscillation due to the free-falling mass impact (m_i=80 g) is captured accurately by Eq. (S48), with the decay time τ_0 =0.7 s and the oscillation period T_0=0.2 s. We further demonstrate that the mass (ranging from 60 to 120 g) will not alter the characteristic damping in the mechanical metamaterial, resulting in a similar decay time of about 0.7 s and the period of oscillations around 0.2 s (Fig. S19b). The impact velocity is obtained by taking the time derivative of Eq. (S48),

$$v(t) = -A_0 e^{-\frac{t}{\tau_0}}\left(\frac{1}{\tau_0}\cos\left(\frac{2\pi}{T_0} + \phi\right) + \frac{2\pi}{T_0}\sin\left(\frac{2\pi t}{T_0} + \phi\right)\right). \tag{S49}$$

Therefore, the ratio between the kinetic energy in the mass E_k (determined by $v(t)$ in Eq. (S49)) and the gravity potential E_{impact} (refer to A_0) for different weights follows $E_k/E_{impact} \sim v^2/gA_0 \sim \cos(\pi t/T_0)$. The oscillation period for the ratio E_k/E_{impact} follows T~T_0/2=0.1 s, consistent with the near-identical phases shown in Fig. 4f.

In contrast to the mechanical metamaterials, the free-falling mass impact in the magnetic metamaterial with Q=1 in the main text does not follow the simple damped harmonic oscillation (Fig. S20). The vibration in the magnetic metamaterial decays exponentially, with a decay time of about 0.25 s, which is only one-third of the metamaterials without magnetic interactions (Fig. S20a). The magnetic metamaterial has a much faster decay of the impact vibration, absorbing most impact energy via the phase transitions. The energy landscape of the metamaterials with Q=1 is modulated by the impact velocity that changes with the impact mass weight, controlling the energy conversion and dissipation events in the falling mass impact. The maximum amplitude of vibrations is also significantly reduced, mitigating the impact of oscillation (Fig. S20b). The mass ceases to vibrate (t > 1 s), while the magnetic metamaterial extends till reaching the quasi-

static equilibrium. The phase boundary between the closed and the open phase propagates after the impact energy is absorbed. As the time scale for the phase boundary propagation is about two orders longer than the impact vibration (10 s compared to 0.1 s in Fig. S20b), the influence of the phase boundary propagation on the impact absorption is negligible. Therefore, the impact energy is mainly dissipated by the closed and open phase transitions instead of the viscous damping observed in the mechanical metamaterial.

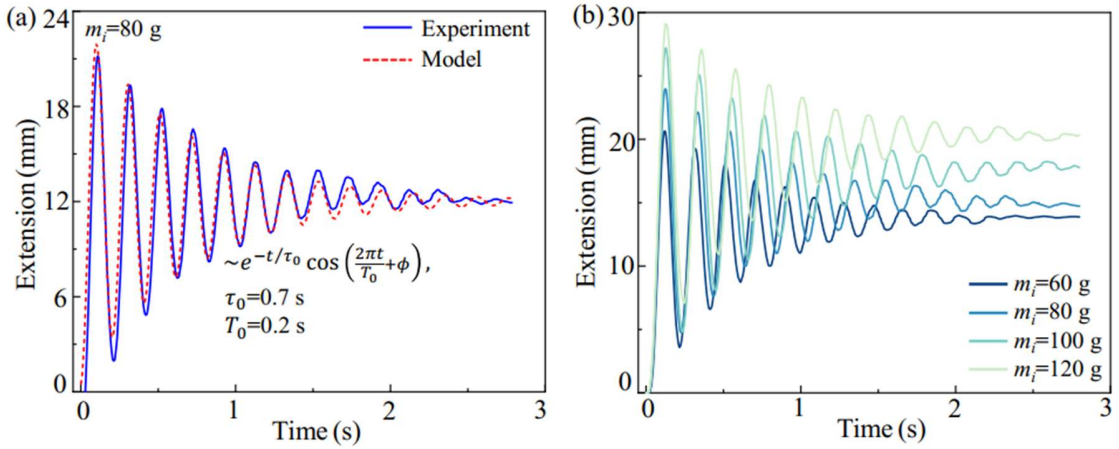

Figure S19. Damped vibrations in the metamaterials with the elliptical pore pattern (w_0=1 mm and a_0=0.17b_0) and no magnetic interaction (Q=0). (a) The metamaterial extension under the free-falling mass impact follows the damped harmonic oscillation, with a decay time of about 0.7 s. (b) Extensions of mechanical metamaterials under different impact masses, ranging from 60 to 120 g. The decay time and oscillation in the mechanical metamaterial remain unchanged for different impact masses.

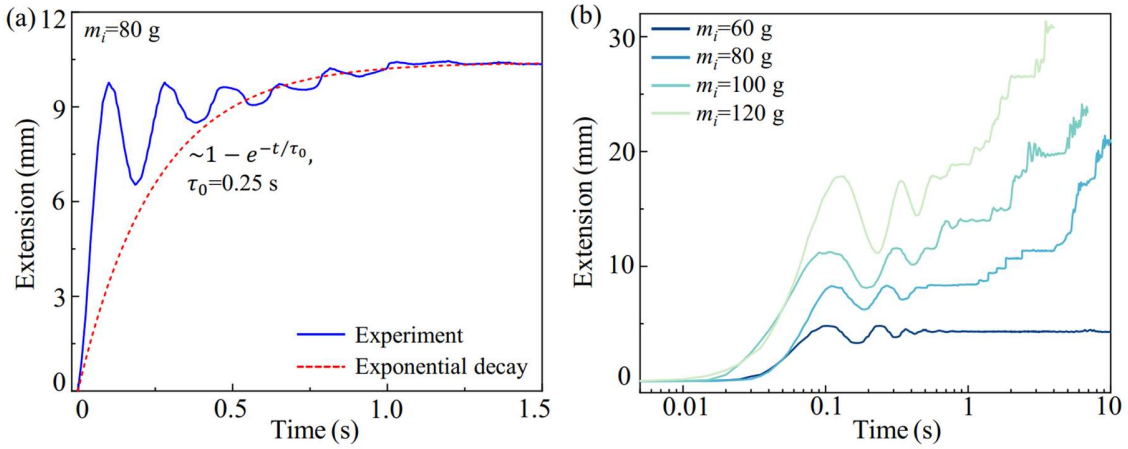

Figure S20. Damped vibrations in the metamaterials with the elliptical pore pattern (w_0=1 mm and a_0=0.17b_0) and attractive magnetic interactions (Q=1). (a) The metamaterial's extension under the free-falling mass impact decays exponentially, with a decay time of about 0.25s. (b) Extensions of elasto-magnetic metamaterials with phase boundary propagations under different impact masses, ranging from 60 to 120 g.

Finally, we demonstrate the rapid decay of the vibration after impact is controlled by the phase transitions in metamaterials instead of the attractive magnetic force. A free-falling mass impacts the metamaterials with the circular pore pattern (w_0=1 mm and a_0=0.97b_0) and the attractive magnetic interaction (Q=1). This metamaterial only supports a single open phase and vibrates with the free-falling mass after impact (Fig. S21a). The oscillation is governed by the contraction and extension of the elastic ligament without causing the pores to collapse. We track the displacement of the impact mass (or the extension of the metamaterial) over time for a mass of 80 g. As shown in Fig. S21b, the displacements follow a damped harmonic oscillation described by Eq. (S48), with the decay time τ_0 =0.36 s and the oscillation period T_0=0.13 s (dashed line).

Even with the attractive magnetic interaction (Q=1), the vibration after impact is similar to the mechanical metamaterials with Q=0 (Fig. S19). We also perform the free-falling mass impact experiments with different weights, ranging from 60 to 120g. The characteristic damped harmonic oscillation in the metamaterial extension (Fig. S21c) and the velocity (Fig. S21d) resemble the damped oscillations, with a similar decay time of about 0.4 s. Therefore, the rapid absorption of the impact energy is induced by the phase transitions in elasto-magnetic metamaterials instead of the attractive magnetic force.

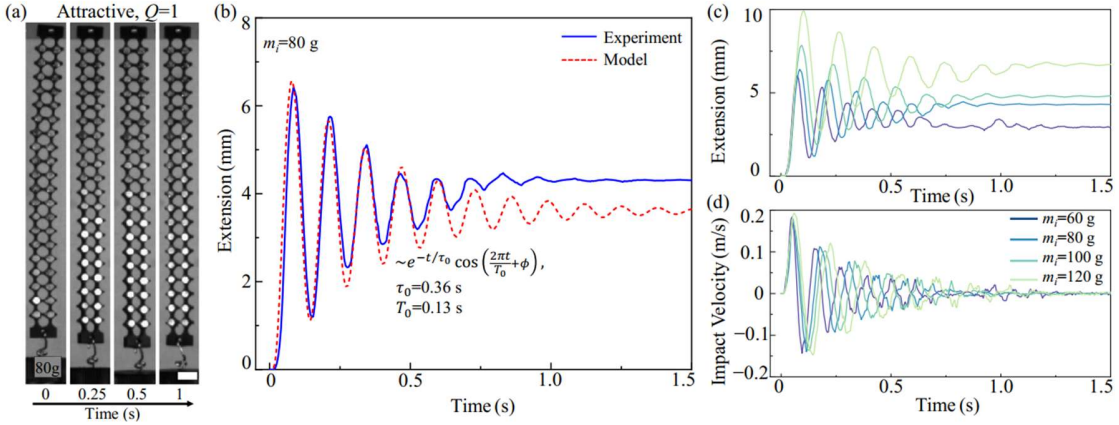

Figure S21. Damped vibrations in elasto-magnetic metamaterials with the circular pore pattern (w_0=1 mm and a_0=0.97b_0) and the attractive magnetic interaction (Q=1). (a) The extension of the metamaterial under free-falling mass impact decays exponentially, with a decay time of about 0.25s. (b) Extensions of elasto-magnetic metamaterials under different impact masses, ranging from 60 to 120 g.

Movie S1. Quasi-static uniaxial loading and loading of elasto-magnetic metamaterials with Q=1, w_0=0.14L_0, and a_0=0.17b_0. A local configuration transitions from closed to open phase emerges at the top and bottom end. It propagates toward the sample's center—the configuration changes to a homogeneous open phase as the deformation increases in the loading cycle. The sample maintains the open phase in the unloading path, ending with a fast transition to the closed phase as the magnets snap to each other within a small distance.

Movie S2. Quasi-static uniaxial loading and loading of elasto-magnetic metamaterials with Q=1, w_0=0.13L_0, and a_0=0.95b_0. A local configuration preserves an open phase, deforming the ligaments in response to external forces. A debonding between the polymer and the magnets is observed as the global strain is larger than 0.2, contributing to the enhanced hysteresis in elasto-magnetic metamaterials with circular pores.

Movie S3. Dynamic recoil of elasto-magnetic metamaterials with Q=1, w_0=0.14L_0, and a_0=0.17b_0. Open-to-closed phase transitions are observed as recoiling is initiated by a trigger at time t =0 ms. The propagations of the phase transitions, superposed to the dynamic recoil, significantly accelerate the recoil velocity. The propagation of the dynamic recoil and the phase transitions travel with different wave speeds governed by the mechanical and magnetic interaction.

Movie S4. Impact in a metamaterial without magnetic domains (Q=0) and elliptical pores a_0=0.17b_0 and w_0=0.14L_0. The free-falling mass hung by the metamaterials is triggered by a customized platform at time t =0 ms. The metamaterial vibrates with a damped harmonic oscillation and dissipates the impact energy. The decay time for the free-falling mass impact is 0.7 s.

Movie S5. Impact in a magnetic metamaterial with attractive magnets (Q=1) and elliptical pores a_0=0.17b_0 and w_0=0.14L_0. The free-falling of a weight hung by the metamaterials is triggered by a customized platform at time t =0 ms. The vibration decays rapidly, with a decay time of about 0.2 s. Elasto-magnetic metamaterials absorbed most of the impact energy via the phase transitions, only returning a small part to the mass for vibrations.

SI References

1. X. Liang, A. J. Crosby, Uniaxial stretching mechanics of cellular flexible metamaterials. *Extreme Mech. Lett.*, **35**, 100637 (2020).
2. X. Liang, A. J. Crosby, Programming impulsive deformation with mechanical metamaterials. *Phys. Rev. Lett.* **125**, 108002 (2020).
3. D. Brown, A. J. Cox, Innovative uses of video analysis. *The Physics Teacher* 47, 145-150 (2009).
4. R. Niu *et al.*, Magnetic handshake materials as a scale-invariant platform for programmed self-assembly. *Proc. Natl. Acad. Sci. USA* **116**, 24402-24407 (2019).
5. V. Nesterenko, Dynamics of heterogeneous materials (Springer Science & Business Media, 2013), pp. 3–13.
6. L. D. Landau, E. M. Lifshitz, Statistical Physics: Volume 5 (Elsevier, 2013), pp. 478–483.
7. P. G. De Gennes, J. Prost, The physics of liquid crystals (Oxford University Press, 1993), pp. 507–527.
8. M. Warner, E. M. Terentjev, Liquid crystal elastomers (Oxford University Press, 2007), pp. 173–183.
9. S. P. Timoshenko, J. M. Gere, Theory of elastic stability (Courier Corporation, 2009), pp. 46-62.
10. R. F. Steildel, Jr., An Introduction to Mechanical Vibrations (John Wiley & Sons, 1989), pp. 164–170.